

Atomically Dispersed CoN₃C₁-TeN₁C₃ Diatomic Sites Anchored in N-doped Carbon as Efficient Bifunctional Catalyst for Synergistic Electrocatalytic Hydrogen Evolution and Oxygen Reduction

Minmin Wang

China University of Petroleum (East China)

Xiuhui Zheng

China University of Petroleum

Min Li

China University of Petroleum (East China)

Kaian Sun

Tsinghua University

Chuhao Liu

Tsinghua University

Weng-Chon Cheong

Department of Chemistry, Tsinghua University

Zhi Liu

China University of Petroleum

Yanju Chen

China University of Petroleum (East China)

Shoujie Liu

Chemistry and Chemical Engineering of Guangdong Laboratory

Bin Wang

Tsinghua University

Yanpeng Li

China University of Petroleum

Yunqi Liu

China University of Petroleum

Chenguang Liu

State Key Laboratory of Heavy Oil Processing, Key Laboratory of Catalysis, China National Petroleum Corp. (CNPC) China University of Petroleum (East China), Qingdao 266555, P. R. China.

Xiang Feng

China University of Petroleum

Chaohe Yang

China University of Petroleum

Yuan Pan (✉ panyuan@upc.edu.cn)

China University of Petroleum

Chen Chen

Tsinghua University

Article

Keywords: hydrogen evolution, oxygen reduction, catalyst

Posted Date: September 23rd, 2021

DOI: <https://doi.org/10.21203/rs.3.rs-907579/v1>

License:  This work is licensed under a Creative Commons Attribution 4.0 International License.

[Read Full License](#)

Atomically Dispersed CoN₃C₁-TeN₁C₃ Diatomic Sites Anchored in N-doped Carbon as Efficient Bifunctional Catalyst for Synergistic Electrocatalytic Hydrogen Evolution and Oxygen Reduction

Minmin Wang^{1,+}, Xiuhui Zheng^{1,+}, Min Li¹, Kaian Sun², Chuhao Liu², Weng-Chon Cheong², Zhi Liu¹, Yanju Chen¹, Shoujie Liu², Bin Wang³, Yanpeng Li¹, Yunqi Liu^{1*}, Chenguang Liu¹, Xiang Feng^{1*}, Chaohe Yang¹, Yuan Pan^{1*}, Chen Chen^{2*}

¹State Key Laboratory of Heavy Oil Processing, China University of Petroleum (East China), Qingdao 266580 (China)

²Department of Chemistry, Tsinghua University, Beijing 100084, China

³School of Chemistry and Chemical Engineering, Shaanxi Normal University, Xi'an 710119 (China)

#These authors contributed equally.

*Correspondence to: liuyq@upc.edu.cn (Y. Liu); xiangfeng@upc.edu.cn (X. Feng); panyuan@upc.edu.cn (Y. Pan); cchen@mail.tsinghua.edu.cn (C. Chen)

Abstract

The development of high atomic economic efficiency catalysts for hydrogen evolution reaction (HER) and oxygen reduction reaction (ORR) are important for the large-scale application of renewable energy technologies but still challenging. Herein, we reported a novel encapsulation-adsorption-pyrolysis strategy for the construction of atomically dispersed Co-Te diatomic sites (DASs) that are anchored in N-doped carbon (N-C) as efficient bifunctional catalyst for synergistic electrocatalytic HER and ORR. The as-constructed catalyst has stable and special $\text{CoN}_3\text{C}_1\text{-TeN}_1\text{C}_3$ coordination structures, $\text{Co}^{\delta+}$ has adsorption-activation function and the neighbouring $\text{Te}^{\delta+}$ acts as an electron donor adjusting the electronic structure of $\text{Co}^{\delta+}$, promoting the dissociation of H_2O molecules and the adsorption of H and oxygen-containing intermediates in HER and ORR. This work provides numerous new opportunities to rational design and artificial synthesis of DASs catalysts for energy conversion.

Introduction

With the problem of energy shortage and environmental pollution becoming more and more serious, it is urgent to develop new clean and renewable energy. Metal-air battery and water splitting are the key for the conversion and storage of green and renewable energy. The electrochemical reactions at the cathode such as hydrogen evolution reaction (HER) and oxygen reduction reaction (ORR) are two important components of water splitting and metal-air battery¹⁻³. The design of high performance HER and ORR bifunctional electrocatalysts is particularly important to improve the efficiency of electrochemical energy conversion. At present, platinum-based catalysts are considered to be the most effective electrocatalysts for the HER and ORR⁴, respectively. However, the high cost and low storage of platinum limit its practical application⁵. Therefore, the development of efficient, low-cost and durable non-noble metal bifunctional electrocatalysts is crucial to improve the efficiency.

Transition metal compounds, such as carbides, phosphides, sulfides and nitrides, have been considered as potential catalytic materials to replace noble metal catalysts⁶⁻⁸. Among them, cobalt-based nanocatalysts (CoS-RGO⁹, CoP@NC/rGO¹⁰, Co/N-GLC¹¹) have attracted much attention in the field of water splitting and zinc-air battery due to their advantages of low price, strong corrosion resistance and good electrocatalytic activity. However, such catalysts have problems such as easy aggregation and low atomic availability still existing in the electrocatalytic reaction process, especially in high-current density and long-period tests. Combining the advantages of heterogeneous and homogeneous catalysts, carbon-supported transition metal single atom catalysts (SACs) have shown excellent electrocatalytic performance by virtue of the characteristic of 100% atom utilization, uniform active site, high conductivity and easy to separate. Fei et al.¹² synthesized Co SACs with Co-N coordination structures, which showed high HER catalytic activity and stability in both acid and alkaline electrolytes. Lyu et al.¹³ synthesized A-Co@CMK-3-D catalyst with content of about 1.52 wt%, which exhibited excellent electrocatalytic ORR activity and

stability in alkaline electrolytes with a half-wave potential of 0.835 V. However, currently reported Co SACs still existing low intrinsic activity and the number of active sites, and most of them are single-functional catalysts. The bifunctional Co SACs with both high HER and ORR performance is rarely reported. Additionally, for HER in alkaline/neutral media, the adsorption and activation of H₂O molecules involve two different atoms (H and O) which are difficult to satisfied by a single atomic site in the Co SACs. Therefore, the proper design of diatomic sites (DASs) catalyst is an effective strategy, which can not only improve the intrinsic activity of Co single atoms, but also achieve synergistic catalysis between different atomic sites. In fact, there are many bimetallic enzymes used for small molecule activation in nature, such as carbon monoxide dehydrogenase (Fe-Mo or Fe-Ni), cytochrome C oxidase (Fe-Cu) and so on. The nature of synergistic catalysis of these bimetallic site enzymes also inspired us to design and synthesize diatomic catalysts. However, the synthesis process of DASs is difficult to accurately control, which makes its rational design and artificial synthesis very challenging. What is more challenging is how to clearly characterize DASs from atomic precision and systematically study its structure-activity relationship and reaction mechanism.

Herein, based on the concept of molecular engineering (ME), we report a atomically dispersed Co-Te diatomic sites catalyst anchored on nitrogen-doped carbon (Co-Te DASs/N-C) with a large specific surface area (1079 m²·g⁻¹) and abundant atomic dispersion sites using an encapsulation-adsorption-pyrolysis strategy. The Co-Te DASs/N-C catalyst has stable coordination structure of CoN₃C₁-TeN₁C₃, Co^{δ+} has adsorption-activation function and the neighbouring Te^{δ+} acts as an electron donor adjusting the electronic structure of Co sites, thus promoting the electrocatalytic performance for both HER and ORR.

Results

As shown in Fig. 1a, based on the concept of molecular engineering, we successfully synthesized a cobalt-tellurium diatomic site catalyst anchored on nitrogen-

doped graphite carbon (Co-Te DASs/N-C) using the encapsulation-adsorption-pyrolysis strategy. The aperture of ZIF-8 is 0.34 nm, the cage diameter is 11.6 nm, and the diameter of Te atom is 0.284 nm, which is smaller than the aperture of ZIF-8, so the Te atoms could be enveloped in the cage of ZIF-8 to obtain Te@ZIF-8 precursor. Then, a layer of tetraphenylporphyrin cobalt (CoTPP) molecules was adsorbed on the surface of ZIF-8 by π - π conjugation to form Te@ZIF-8@CoTPP with a sandwich-like structure. After pyrolysis at 920°C under N₂, the intermediate layer ZIF-8 was carbonized to form a nitrogen-doped carbon substrate, and Zn volatilized at high temperature. Te atoms in the cage diffused outward from the channel of ZIF-8 to the intermediate carbon layer, while the outer Co atoms migrated to the intermediate carbon layer. The Te and Co atoms were anchored by N and C atoms at the same time, forming a stable diatomic site catalyst with CoN₃C₁-TeC₃N₁ coordination structure and large specific surface area. As a comparison, we synthesized Co SASs/N-C and Te SASs/N-C catalyst (Fig. S1, S2). Inductively coupled plasma (ICP) result (Table 2) shows that the the Co loading of Co-Te DASs/N-C is 0.37 wt%.

X-ray diffraction patterns (XRD) (Fig. S3) only shows two broad graphite carbon peaks at 25° and 44°,^{14,15} which indicated that Co and Te atoms are highly dispersed on the N-C. The Raman spectrum (Fig. S4) shows the D band peak at 1350 cm⁻¹ and the G band peak at 1600 cm⁻¹. The D band peak reflects the defect degree of the catalysts, and the G band peak reflects the graphitization degree¹⁶⁻¹⁸. Compared with Co SASs/N-C ($I_D/I_G = 0.98$) and Te SASs/N-C ($I_D/I_G = 1.0$), the Co-Te DASs/N-C catalyst shows the lowest I_D/I_G value of 0.95, indicating higher graphitization degree and better electrical conductivity.

A uniform polyhedron morphology can be observed from scanning electron microscope (SEM) (Fig. 1b) and transmission electron microscopy (TEM) (Fig. 1c) of Co-Te DASs/N-C catalyst. No particles can be found in the TEM images. The ring-like selected area electron diffraction (SAED) pattern demonstrated its poor crystallinity (Fig. 1c). Energy-dispersive X-ray spectroscopy (EDS) mapping images reveal that Co, Te, C and N elements are homogeneously distributed on the N-C (Fig. 1f). The SEM

and TEM of the Co SASs/N-C and Te SASs/N-C catalyst have similar morphology to Co-Te DASs/N-C (Fig. S7-S9). No particles can be observed, indicating that Co and Te atoms are highly dispersed on the N-C. A large number of evenly dispersed single atoms can be observed by spherical aberration corrected high-angle annular dark-field scanning transmission electron microscopy (AC-HAADF-STEM) (Fig. 1d and Fig. S9d). In order to further confirm the existence of Co and Te atoms, AtomSegNet App was used to conduct super-resolution processing and tracking of atomic features in AC-HAADF-STEM images^{19,20}. The bright spots of uniform size can be observed in the atom detect image of Te SASs/N-C (Fig. S9e). Meanwhile, the image of Co-Te DASs/N-C shows two kind of bright spots with different sizes, the larger ones represent Te atoms and the smaller ones represent Co atoms (Fig. 1e), demonstrating the Co and Te atoms co-exist in the Co-Te DASs/N-C catalyst.

X-ray photoelectron spectroscopy (XPS) was used to characterize the element composition and valence of the catalyst (Fig. S10-S11). XPS surveys result reveals the presence of Co, Te, C and N elements. The peaks of Co 2p_{3/2} and Co 2p_{1/2} located at 780.1 and 796.3 eV in Co 2p spectrum (Fig. S10a), which can be attributed to Co²⁺.^{21,22} The Te 3d_{5/2} peak located at 573.8 eV and Te 3d_{3/2} peak located at 584 eV could be assigned to Te^{δ-}. The peaks located at 575.7 eV and 585.9 eV in the Te 3d_{5/2} and Te 3d_{3/2} spectrum, respectively, which can be attributed to Te⁴⁺ (Fig. S10b)^{23,24}. The C 1s XPS spectrum (Fig. S10d) showed three peaks with binding energies of 288.2, 285.6 and 284.2 eV, which were attributed to O=C-O, C=N and C=C, respectively. The N 1s XPS spectrum (Fig. S10c) can be divided into four different types of N including pyridinic N (398.2 eV), Co-N (399.6 eV), pyrrolic N (400.4 eV) and graphitic N (401.3 eV)^{12,15,25}. And pyridinic N occupies the dominant percentage of N species, which may play the vital role as active sites for the HER²⁶ and ORR^{27,28}. From the ultraviolet photoelectron spectroscopy (UPS) (Fig. 1g), the maximum valence band of Co SASs/N-C is 1.9 eV, while that of Co-Te DASs/N-C is -0.5 eV, indicating the *d*-band center of Co-Te DASs/N-C is shifted towards Fermi level. This further indicates that the addition of Te changes the electronic environment of Co and reduces the valence state of Co.

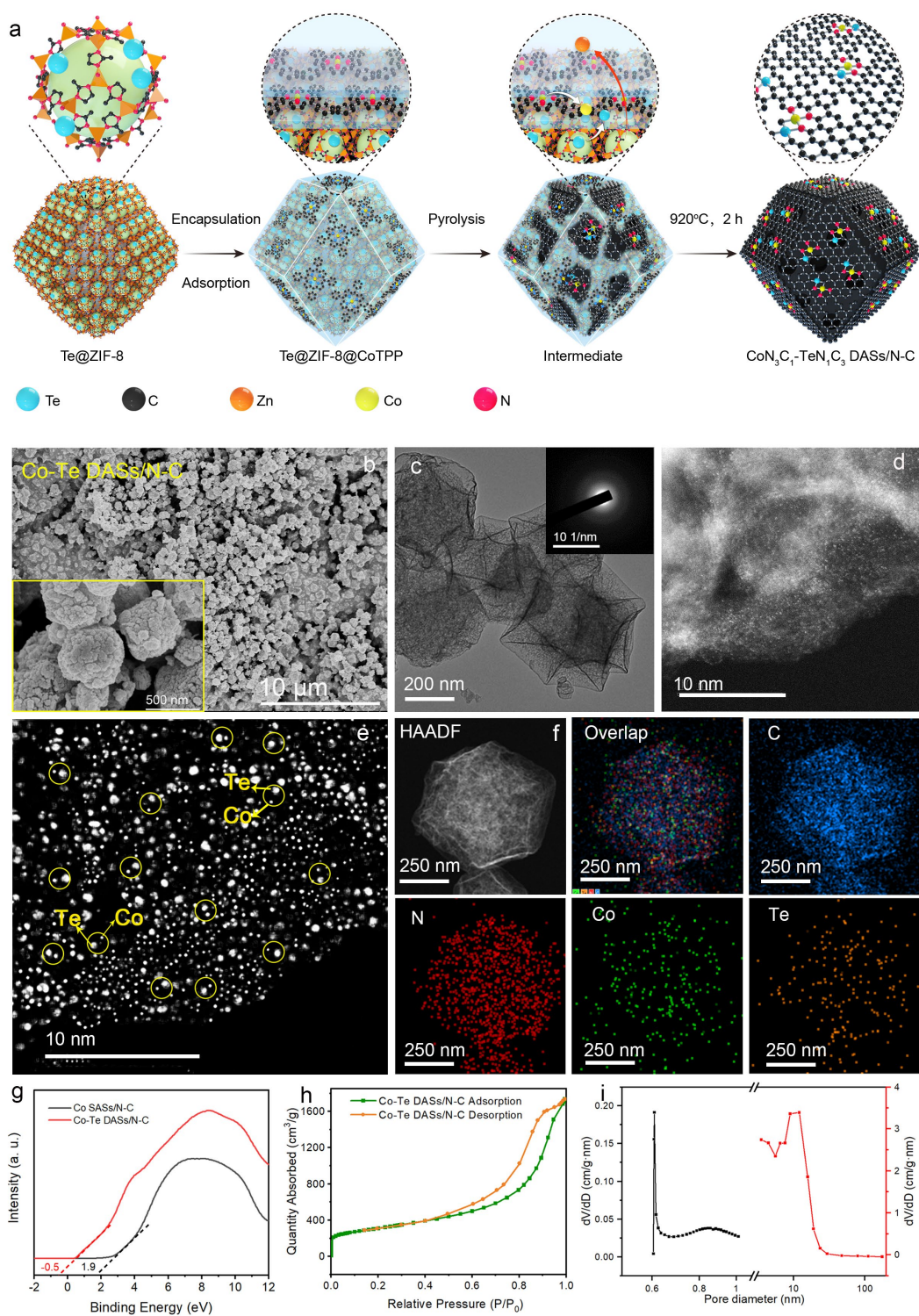


Fig. 1. Synthesis and structure characterization of Co-Te DASs/N-C catalyst. (a) Schematic illustration of the synthesis process, (b) SEM, (c) TEM (the inset is SAED image), (d) AC-HAADF-STEM, (e) the treatment of (d) by AtomSegNet App, (f) EDS mapping, (g) UPS spectrum, (h) N_2 adsorption–desorption isotherm, (i) the pore size distribution.

The pore structure information of the Co-Te DASs/N-C catalyst was characterized by N₂ absorption/desorption. The typical type IV isotherm with a distinct hysteresis loop can be observed (Fig. 1h). The Co-Te DASs/N-C catalyst shows a large Brunner–Emmet–Teller (BET) surface area of 1079 m²·g⁻¹, which is larger than that of the Co SASs/N-C (727 m²·g⁻¹) and the Te SASs/N-C (457 m²·g⁻¹) (Fig. S5, S6). Besides, the pore sizes are mainly concentrated at 0.52 and 16 nm, respectively (Fig. 1i). The large specific surface area and porous structure can provide abundant exposed active sites, and promote charge and mass transport during the electrocatalytic process²⁹.

X-ray absorption near-edge structure (XANES) and extended X-ray absorption fine structure (EXAFS) spectrum were used to further understand the electron structure and coordination environment of Co and Te atoms in Co-Te DASs/N-C catalyst³⁰. The Co absorption edge of Co-Te DASs/N-C is located between CoO and Co foil, suggesting the valence state of Co atom is between 0 and +2 (Fig. 2a). The absorption threshold energies (E₀) can be obtained from the first derivative, the E₀ value of Co in Co foil, CoO, Co₃O₄, Co SASs/N-C, Co-Te DASs/N-C are 7708.3, 7721.0, 7728.1, 7722.5, 7714.7 eV, respectively. The E₀ of Co-Te DASs/N-C is smaller than that of the Co SASs/N-C, indicating the oxidation state of Co in Co-Te DASs/N-C decreases (Fig. 2b). The average valence state of Co in Co-Te DASs/N-C is +0.9, lower than that of Co (+2.1) in Co SASs/N-C (Fig. 2c). The Fourier-transformed (FT) k³-weighted EXAFS spectrum of the Co-Te DASs/N-C catalyst shows a main peak at 1.5 Å, corresponding to the Co-N(C) of first coordination shell, and no Co-Co coordination peak at 2.2 Å can be observed. Besides, there is a peak at 2.5 Å belonging to the Co-Te of second coordination layer (Fig. 2g). In addition, the Co-N coordination peak strength of Co-Te DASs/N-C in R space is lower than that of Co SASs/N-C, illustrating the coordination number of Co-N decreases. The wavelet transform (WT) plot of Co-Te DASs/N-C shows the WT maximum at 4 Å⁻¹, corresponding to the Co-N(C) by comparing with Co foil, CoO and Co₃O₄ (Fig. 2m). By EXAFS fitting of Co (Fig. 2i-j, S12-S14), the Co-N coordination numbers of Co SASs/N-C and Co-Te DASs/N-C catalysts are 4 and 3, respectively, and the Co-C coordination number of the Co-Te DASs/N-C catalyst is 1 (Table S3).

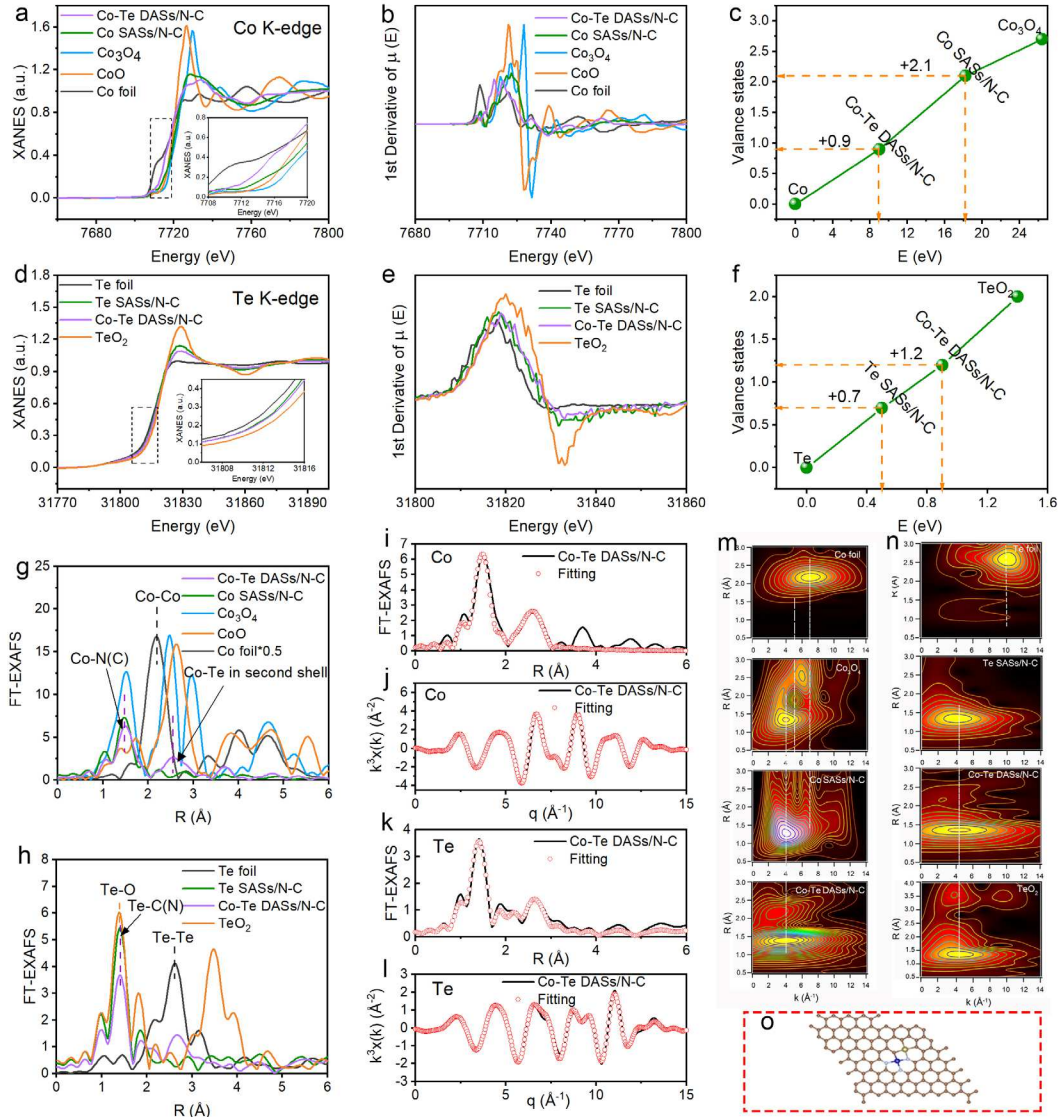


Fig. 2. Electronic structures and local chemical configurations of Co-Te DASs/N-C catalyst. (a, d) XANES of Co K-edge and Te K-edge, (b, e) the first derivatives of the Co K-edge and Te K-edge, (c, f) the fitted average oxidation states of Co and Te from XANES spectra, (g, h) k^3 -weighted Fourier transform (FT) spectra of Co and Te at R spaces, (i-l) EXAFS fitting in R and q spaces, (m, n) WT contour plots, (o) the structure model of Co-Te DASs/N-C catalyst.

The Te absorption edge of the Co-Te DASs/N-C is located between Te foil and TeO₂, suggesting Te carries a positive charge and the valence state of Te is between 0 and +4 (Fig. 2d). From the first derivative of XANES of Te K-edge, the peak of Co-Te DASs/N-C towards the direction of high energy compared with the Te SAs/N-C, suggesting the oxidation state of Te in Co-Te DASs/N-C catalyst increases (Fig. 2e).

The average valence state of Te in Co-Te DASs/N-C is +1.2, higher than that of Te (+0.7) in Te SASs/N-C (Fig. 2f). From the FT k^3 weighted EXAFS spectrum, there is a main peak at 1.2 Å corresponding to the Te-C(N) coordination (Fig. 2h). The WT plots of Co-Te DASs/N-C shows the maximum at about 4.2 Å⁻¹, corresponding to the Te-N(C) coordination by comparing with Te foil, TeO₂ and Te SASs/N-C (Fig. 2n). By fitting EXAFS (Fig. 2k-l, S15-S17), the Te-C coordination numbers of Co-Te DASs/N-C and Te SASs/N-C are 3 and 4, respectively, and the Te-N coordination number of Co-Te DASs/N-C is 1. In the C K-edge spectrum (Fig. S18), the peak C1 at 285.4 eV and peak C3 at 293 eV is caused by the excitation of π^* and σ^* , which can be attributed to C-C species, respectively. The C2 peak at 288.4 eV indicates the formation of C-N-C. Besides, the C2 peak of Co-Te DASs/N-C is shifted to the left compared with the peak of Co SASs/N-C (Fig. S19), which is caused by doping of Te. These results further indicate that Te atoms are successfully doped into the N-C³¹. Therefore, the Co-Te DASs/N-C exists diatomic CoN₃C₁-TeN₁C₃ center connected by N-C, in which the Co and Te atoms connect to the N and C atoms in N-C. It is speculated that the central structure of Co SASs/N-C and Te SASs/N-C consists of single atom Co-N₄ and Te-C₄ (Fig. S32) centers connected by N-C.

The HER performance was examined in 1 M KOH and 0.5 M H₂SO₄ using a typical three-electrodes system. We first evaluated the electrocatalytic activity of a series of Co-Te DASs/N-C catalysts with different Co and Te contents (Fig. S20, S21). The Co-Te DASs/N-C catalyst with Co/Te ratio of 0.1/1 shows the best electrocatalytic HER activity. For comparison, a series of reference samples, including 20% Pt/C, CN, Co SASs/N-C and Te SASs/N-C catalysts were also investigated. For HER, when the current density reaches 10 mA·cm⁻², Co-Te DASs/N-C needs overpotentials of 217 and 246 mV (vs. RHE) in 1 M KOH (Fig. 3b) and 0.5 M H₂SO₄ (Fig. 3a), which are lower than Co SASs/N-C (426 and 442 mV) and Te SASs/N-C (651 and 476 mV) catalyst. The Tafel slopes of Co-Te DASs/N-C catalyst in 1 M KOH (Fig. S22b) and 0.5 M H₂SO₄ (Fig. S22a) are 76.8 and 89.3 mV·dec⁻¹, respectively, which are smaller than that of Co SASs/N-C (132.2 and 157.3 mV·dec⁻¹) and Te SASs/N-C (256.9 and 173.3 mV·dec⁻¹). The Tafel slopes of the Co-Te DASs/N-C catalyst also suggest that the rate-

controlling step is volmer step and the HER process is Volmer–Heyrovesky pathway⁷. The turnover frequencies (TOFs) are then calculated (Fig. S24, S28). In order to achieve the overpotential of 300 mV, the TOFs of Co-Te DASs/N-C are 0.32 and 0.23 s⁻¹ in 1 M KOH and 0.5 M H₂SO₄, respectively, which are higher than that of Co SASs/N-C (0.02 and 0.04 s⁻¹) and Te SASs/N-C (0.004 and 0.009 s⁻¹) catalysts, indicating the highest intrinsic activity of Co-Te DASs/N-C catalyst.

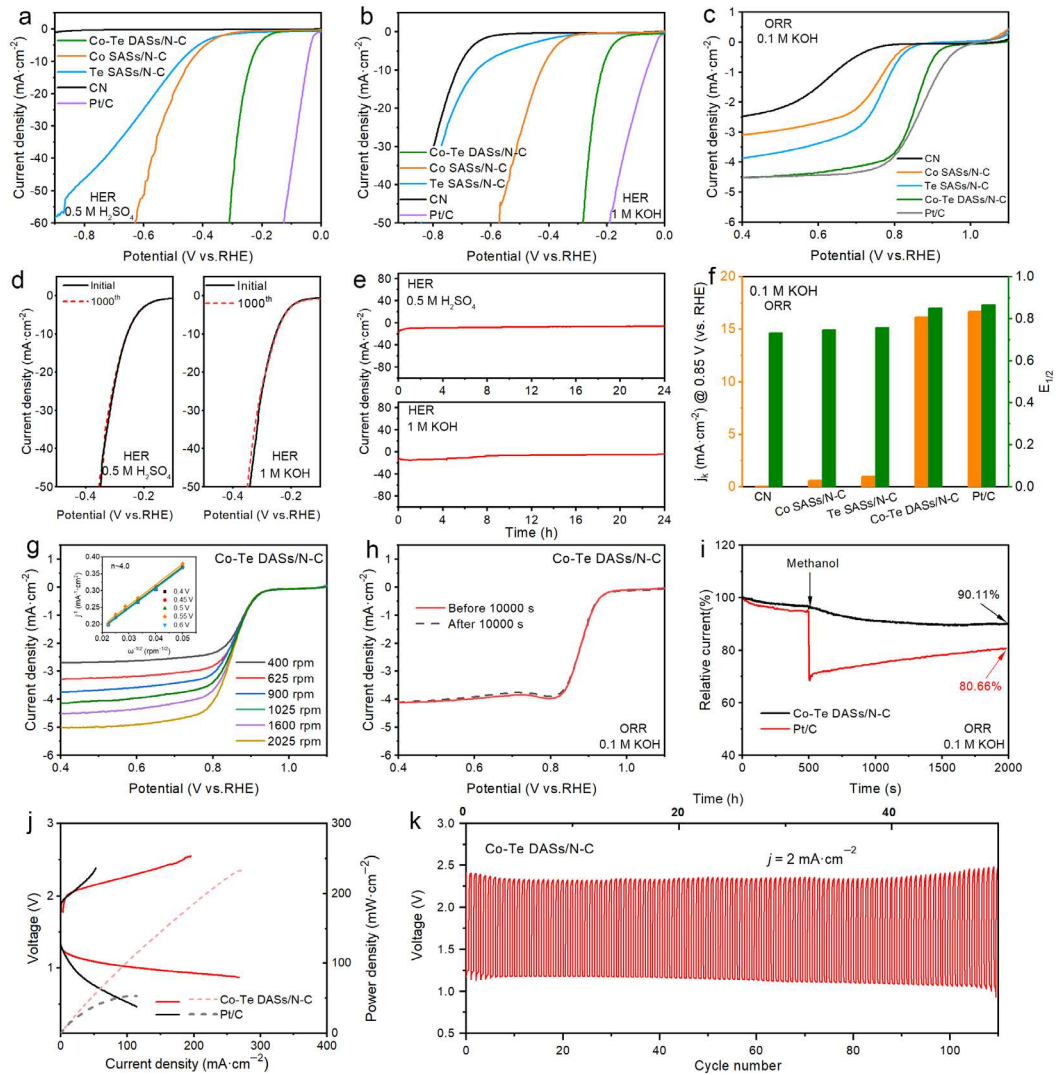


Fig. 3. Electrocatalytic HER and ORR performances. LSV curves for HER in (a) 0.5 M H₂SO₄, (b) 1 M KOH, (c) LSV curves for ORR in 0.1 M KOH, (d) LSV curves of Co-Te DASs/N-C before and after durability tests, (e) i-t plot curves, (f) j_k at 0.85 V and $E_{1/2}$, (g) LSV curves of Co-Te DASs/N-C at different rotation speeds (insets shows the corresponding K-L plots), (h) LSV curves before and after durability test for 10000

s, (i) methanol tolerance tests (~1.0 M methanol), (j) charge–discharge polarization curve and power density plot, (k) charge–discharge cycling performance.

The electrochemical active surface area (ECSA) of the catalysts is reflected from the double-layer capacitance (C_{dl}). The C_{dl} values of the Co-Te DASs/N-C are 22.5 and 23.1 $\text{mF}\cdot\text{cm}^{-2}$ in 1 M KOH and 0.5 M H_2SO_4 , respectively, which are higher than that of NC, Co SASs/N-C and Te SASs/N-C catalysts (Fig. S25), indicating the larger ECSA of Co-Te DASs/N-C. The Co-Te DASs/N-C catalyst shows the lowest charge transfer resistance (R_{ct}) compared with the NC, Co SASs/N-C and Te SASs/N-C catalysts (Fig. S23), suggesting its rapid charge transport, which can be attributed to the porous structure and the large BET surface area. After 1000 cycles, the polarization curves of Co-Te DASs/N-C remain unchanged in 0.5 M H_2SO_4 and 1 M KOH (Fig. 3d). In addition, the Co-Te DASs/N-C shows excellent stability in long-term electrochemical process, maintaining at least 24 h in 1 M KOH and 0.5 M H_2SO_4 , respectively (Fig. 3e). Additionally, the Co-Te DASs/N-C catalyst also shows excellent catalytic activity and stability in the PBS solution ($\text{pH} = 7$) (Fig. S26-S27). Therefore, the Co-Te DASs/N-C catalyst can achieve efficient hydrogen evolution in a wide pH range ($\text{pH} = 0\sim 14$).

We further measured the catalytic ORR performance in 0.1 M KOH electrolyte with a rotating disk electrode (RDE). In O_2 saturated 0.1 M KOH, the Co-Te DASs/N-C catalyst shows a comparable ORR activity to Pt/C with $E_{1/2}$ of 0.852 V, which is better than that of Co SASs/N-C ($E_{1/2}\sim 0.819$ V) and Te SASs/N-C ($E_{1/2}\sim 0.758$ V), and CN manifests the worst ORR catalytic activity (Fig. 3c, S30). The kinetic current density (J_k) at 0.85 V (vs. RHE) for Co-Te DASs/N-C ($16.16 \text{ mA}\cdot\text{cm}^{-2}$) is higher than that of Co SASs/N-C ($1.04 \text{ mA}\cdot\text{cm}^{-2}$), Te SASs/N-C ($0.98 \text{ mA}\cdot\text{cm}^{-2}$) and CN ($0.03 \text{ mA}\cdot\text{cm}^{-2}$) (Fig. 3f). The Tafel slopes are 62.3, 54.0, 68.5, 70.1 and 140.9 $\text{mV}\cdot\text{dec}^{-1}$ for Co-Te DASs/N-C, Pt/C, Co SASs/N-C, Te SASs/N-C and CN, respectively, indicating faster kinetics of Co-Te DASs/N-C (Fig. S31). The electron transfer number (n) is calculated to be about 4 (Fig. 3g, S29), revealing the high ORR selectivity and efficient $4e^-$ transfer mechanism^{32,33}. In addition, the Co-Te DASs/N-C catalyst shows good long-term stability. After 10,000 s continuous working, the E_{onset} and $E_{1/2}$ of Co-Te

DASs/N-C catalyst nearly not change (Fig. 3h). Meanwhile, the Co-Te DASs/N-C catalyst also shows excellent tolerance to methanol, Co-Te DASs/N-C displays a very high current retention rate of 90.11% after 2000 s, while commercial Pt/C encounters a sudden current drop when methanol is added at 500 s, and only shows a current retention rate of 80.66% (Fig. 3i). In order to evaluate the activity and durability of Co-Te DASs/N-C catalyst in practical applications, the Co-Te DASs/N-C catalyst is applied in homemade Zn-air batteries. The voltage gap between discharge and charge is 1.06 V at $50 \text{ mA}\cdot\text{cm}^{-2}$ for the Co-Te DASs/N-C based battery, which is lower than that of Pt/C (1.58 V at $50 \text{ mA}\cdot\text{cm}^{-2}$). The Co-Te DASs/N-C based Zn-air battery shows a larger power density of $233 \text{ mW}\cdot\text{cm}^{-2}$ at $271 \text{ mA}\cdot\text{cm}^{-2}$ than that of Pt/C ($53 \text{ mW}\cdot\text{cm}^{-2}$ at $110 \text{ mA}\cdot\text{cm}^{-2}$) (Fig. 3j, S35a), confirming the high ORR activity in real Zn-air battery. Besides, the Co-Te DASs/N-C based battery exhibits excellent stability without obvious voltage change after 110 cycles (50 h, Fig. 3k), it also displays a discharge specific capacity of $796.1 \text{ mA h g}^{-1}$, higher than that of Pt/C ($744.7 \text{ mA h g}^{-1}$) (Fig. S35b).

The spin-polarized DFT calculation was further performed to understand the higher ORR and HER performance of the Co-Te DASs/N-C catalyst (Fig. 4, Fig. S32-S34). Based on the XAS results, the four stable catalytic structure models of CN, CoN_4 , TeC_4 and $\text{CoN}_3\text{C}_1\text{TeN}_1\text{C}_3$ were constructed, and can be used to represent CN, Co SASs/N-C, Te SASs/N-C and Co-Te DASs/N-C, respectively (Table S1, Fig. S32 and Fig. 2o). According to the ORR free energy diagrams in Fig. 4d, the theoretical overpotential of Co-Te DASs/N-C is 0.31 V, which is superior to that of CN (0.78 V), Te SASs/N-C (0.67 V), and Co SASs/N-C (0.34 V). The potential determining step (PDS) of Co SASs/N-C is the final step (from OH^* to OH^-), while the PDS of the other three catalysts is the first step (from O_2 to OOH^*). Therefore, Co-Te DASs/N-C has the lowest theoretical overpotential and the highest theoretical limiting potential by reducing the adsorption strength of OH ($\Delta G_{\text{H}^*} = 0.18 \text{ eV}$) compared with Co SASs/N-C ($\Delta G_{\text{H}^*} = 0.12 \text{ eV}$). In addition, to elucidate the HER theoretical performance in both acid and alkaline media, the Gibbs free energy of H adsorption (ΔG_{H^*}) and water dissociation kinetic energy barrier were further calculated. The ΔG_{H^*} of Co-Te

DASs/N-C is 0.09 eV, which is closer to 0 eV and lower than that of the CN (1.1 eV), Te SASs/N-C (0.29 eV) and Co SASs/N-C (0.15 eV) catalysts, strongly indicating the enhanced H adsorption kinetics in Co-Te DASs/N-C (Fig. 4a).

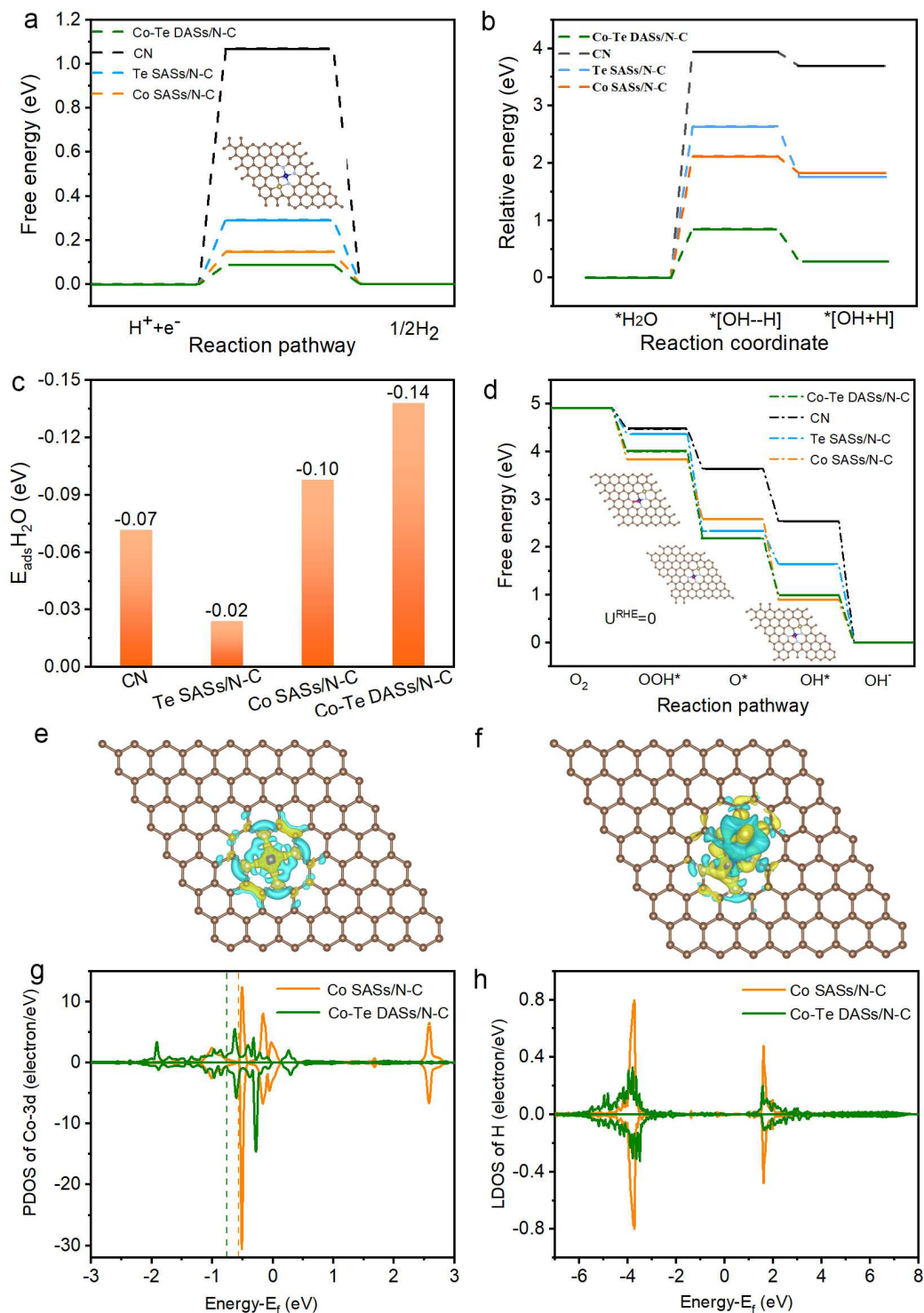


Fig. 4. DFT calculations. (a) The calculated ΔG_{H^*} for different catalysts in the acidic HER process, (b) the dissociation reaction energy diagrams of H₂O molecule in different catalysts, (c) the adsorption energy (E_{ads}) for H₂O adsorption and dissociation, (d) the free energy diagram for O₂ reduction, (e, f) the charge density isosurfaces of Co-Te DASs/N-C and Co SASs/N-C, (g, h) the partial density of states (PDOS) and local density of states (LDOS) of Co-3d and H, respectively.

(d) the ORR free energy diagrams in different catalysts, (e) Charge density difference of Co SASs/N-C, (f) charge density difference of Co-Te DASs/N-C, (g) the PDOS diagrams of the 3d orbitals of Co atom in Co SASs/N-C and Co-Te DASs/N-C, (h) the LDOS diagrams of H atom after H adsorption in Co SASs/N-C and Co-Te DASs/N-C.

Besides, the lowest water dissociation kinetic energy barrier in the Co-Te DASs/N-C catalyst (0.85 eV) indicates the fastest water dissociation step compared with that of the CN (3.94 eV), Te SASs/N-C (2.63 eV) and Co SASs/N-C (2.11 eV) catalysts. And the enhanced dissociation capability of H₂O molecule in the Co-Te DASs/N-C catalyst should be ascribed to its higher adsorption energy(-0.14 eV) compared with that of the CN (-0.07 eV), Te SASs/N-C (-0.02 eV) and Co SASs/N-C (-0.10 eV) catalysts (Fig. 4c). This further proves the boosted alkaline HER performance of the Co-Te DASs/N-C catalyst (Fig. 4b).

The electronic structure calculations were further used to elucidate the moderate interactions between active sites and adsorbates in all the catalysts. According to the Bader charge analysis and the *d*-band center calculation (Fig. 4e, 4f, 4h), the electrons are transferred from Te atom to Co atom in the Co-Te DASs/N-C catalyst, and thus the *d*-band center of Co atom in Co-Te DASs/N-C (-0.76) is lower than that of in Co SASs/N-C (-0.56). Therefore, the electron transfer leads to the downshift of *d*-band center of Co atom, thus weakening the adsorption of oxygen-containing intermediates (i.e., OH*, OOH*, O*)³⁴. In the acidic HER process, the Co-Te DASs/N-C catalyst can provide more active surface states to interact with H according to the PDOS diagram. This shifts the bonding states to lower energy and the anti-bonding states to higher energy (Fig. 4g). In addition, it causes the originally localized H atom state to become more delocalized due to the strengthening of the orbital hybridization. This significantly promotes the adsorption of H^{35,36}. In the alkaline HER process, the more obvious molecular orbitals broadening and mixing near the Fermi level, as well as the downshift of these molecular orbitals away from the Fermi level, also indicate the strongest activation of the H₂O molecule on the Co-Te DASs/N-C catalyst (Fig. S34). Therefore, the synergistic effect between the atomic Co and Te promotes the electron transfer from Te to Co, and also modifies the electronic structure of Co. This results in the weakening

of the OH adsorption and enhancement of H and H₂O adsorption for the Co-Te DASs/N-C catalyst, and thus the significantly boosted ORR and HER performance.

Discussion

In summary, the Co-Te DASs/N-C catalyst is successfully synthesized by a novel encapsulation-adsorption-pyrolysis strategy, and there are diatomic active centers (CoN₃C₁-TeN₁C₃) in the catalyst which are favorable for HER and ORR. In Co-Te DASs/N-C catalyst, the Co^{δ+} sites have adsorption-activation function and the neighbouring Te^{δ+} sites act as an electron donor adjusting the electronic structure of Co sites, thereby exhibiting superior bifunctional electrocatalytic performances for both HER and ORR. DFT further reveals the electron transfer from Te to Co atoms promotes the dissociation of H₂O molecules and the adsorption of H and oxygen-containing intermediates, thus accelerating the HER and ORR process. This work not only provides new opportunities for the development of novel diatomic active site catalysts for advanced energy conversion, but also proves that semi-metallic regulation is efficient strategy for improving the intrinsic activity of transition metals single atom catalysts.

Methods

Synthesis of Te@ZIF-8 with different Te content. For the synthesis of Te@ZIF-8 with different Te content, Zn(NO₃)₂·6H₂O (5.58 g, 0.02 mol) and 1 g of Te powder were dissolved in 150 mL methanol to form solution A. The MeIm (6.16 g, 0.075 mol) was dissolved in 150 mL methanol to form clear solution B. Then, the solution B was subsequently poured into the solution A. After mixing and stirring at room temperature for 24 h, the precipitate was centrifuged and washed with water and ethanol several times and dried at 60 °C. By changing the addition content of Te powder, Te@ZIF-8 with different Te content can be obtained.

Synthesis of CoTe@ZIF-8. In a typical synthesis of CoTe@ZIF-8, 0.5 g of Te@ZIF-8 was dissolved in 50 mL DMF to form solution A. The cobalt tetraphenylporphyrin was

dissolved in 50 mL DMF to form solution B. Then, the solution B was subsequently poured into the solution A. After mixing and stirring at room temperature for 24 h, the precipitate was centrifuged and washed with water and ethanol several times and dried at 60 °C. By changing the addition content of cobalt tetraphenylporphyrin, CoTe@ZIF-8 with different Co content can be obtained.

Synthesis of Co-Te DASs/N-C. For the synthesis of Co-Te DASs/N-C catalyst with different Co content, the CoTe@ZIF-8 with different Co content composites were placed in a tube furnace and heated to 920 °C with a ramp rate of 2 °C·min⁻¹ and kept for 2 h in flowing N₂ and the black powder was obtained.

Synthesis of ZIF-8. In a normal procedure, Zn(NO₃)₂·6H₂O (5.58 g) was dissolved in 150 mL of methanol; then 2-methylimidazole (6.16 g) in 150 mL of methanol was subsequently injected into above solution under vigorously stirring for 24 h at room temperature. The obtained precipitates were centrifuged and washed with water and ethanol several times and dried in vacuum at 60 °C for overnight.

Synthesis of Co@ZIF-8. In a normal procedure, 0.5 g ZIF-8 were dissolved in 50 mL of DMF to form solution A; then cobalt tetraphenylporphyrin was dissolved in 50 mL DMF to form solution B, the solution B was subsequently injected into the solution A under vigorously stirring for 24 h at room temperature. The as-obtained precipitates were centrifuged and washed with water and ethanol several times and dried in vacuum at 60 °C for overnight.

Synthesis of Co SASs/N-C. For the synthesis of Co SASs/N-C catalyst, the Co@ZIF-8 were placed in a tube furnace and heated to 920 °C with a ramp rate of 2 °C·min⁻¹ and kept for 2 h in flowing N₂ and the black powder was obtained.

Synthesis of Te SASs/N-C. For the synthesis of Te SASs/N-C catalyst, the CoTe@ZIF-8 were placed in a tube furnace and heated to 920 °C with a ramp rate of 2 °C·min⁻¹ and kept for 2 h in flowing N₂ and the black powder was obtained.

Synthesis of CN. For the synthesis of NC catalyst, the ZIF-8 were placed in a tube furnace and heated to 920 °C with a ramp rate of 2 °C·min⁻¹ and kept for 2 h in flowing N₂ and the black powder was obtained.

Electrochemical test

To prepare the working electrode, a total of 5 mg of the electrocatalyst and 20 μl of 5 wt% Nafion solution were dispersed in 1 ml ethanol. 20 μl of the ink were dropped onto the glassy carbon electrode, which was allowed to dry at room temperature. The three-electrode system consists of a working electrode, a carbon rod counter electrode and a saturated calomel reference electrode (SCE) or Ag/AgCl reference electrode. The electrochemical tests were conducted in N_2 -saturated 1 M KOH/0.5 M H_2SO_4 for the HER at room temperature. The electrocatalytic activity of the samples was examined by obtaining polarization curves using linear sweep voltammetry (LSV) with a scan rate of $5 \text{ mV}\cdot\text{s}^{-1}$ at room temperature. Alternating current impedance tests were performed at different potentials from 10^5 to 0.1 Hz. The stability measurements were performed by cyclic voltammetry and chronoamperometry. Cyclic voltammetry (CV) method also was used to determine the electrochemical double-layer capacitances (C_{dl}). Electrochemically active surface area could be evaluated from the slope of the plot of the charging current versus the scan rate, which was directly proportional to C_{dl} .

The ORR measurements were performed in an O_2 saturated 0.1 M KOH solution in a standard three-electrode setup using a rotating disk electrode at room temperature. The platinum electrode was used as the counter electrode and saturated calomel electrode (SCE) were employed as the reference electrode. A glassy carbon (GC) electrode (0.196 cm^2) served as the substrate for the working electrode. The LSV tests were measured at various rotating speed from 425 to 2025 rpm with a sweep rate of $5 \text{ mV}\cdot\text{s}^{-1}$. The cyclic voltammetry (CV) were carried out at the scan rate of $40 \text{ mV}\cdot\text{s}^{-1}$. Stability test were conducted with a rotation rate of 1600 rpm. The electron transfer number (n) and kinetic current density (J_k) can be calculated from Koutecky-Levich equation:

$$\frac{1}{J} = \frac{1}{J_L} + \frac{1}{J_K} = \frac{1}{B\omega^{1/2}} + \frac{1}{J_K}$$

$$B = 0.2nFC_{O_2}D_{O_2}^{2/3}\nu^{-1/6}$$

where J , J_L and J_k are the measured current density, limiting current density and kinetic current density, respectively. B is the inverse of the slope of K-L equation. ω is the angular velocity of the disk, n is the electron transfer number, F is the Faraday

constant ($96485 \text{ C}\cdot\text{mol}^{-1}$), C_{O_2} is the bulk concentration of O_2 ($1.2 \times 10^{-6} \text{ mol}\cdot\text{cm}^{-3}$), D_{O_2} is the diffusion coefficient of O_2 in 0.1 M KOH ($1.9 \times 10^{-5} \text{ cm}^2\cdot\text{s}^{-1}$), and ν is the kinematic viscosity of the electrolyte ($0.01 \text{ cm}^2\cdot\text{s}^{-1}$).

All the measured potentials in this work were performed with iR compensation and were converted to reverse hydrogen electrode (RHE) by the following equations:

$$E_{RHE} = E_{Ag/AgCl} + 0.059pH + 0.197$$

$$E_{RHE} = E_{SCE} + 0.059pH + 0.241$$

Turnover frequency (TOF) calculations

Cyclic voltammetry (CV) curves were measured at $5 \text{ mV}\cdot\text{s}^{-1}$ in phosphate buffered saline solution (PBS, pH = 7.0). The quantity of active species (N) and TOF values are calculated according to the following formula:

$$N = \frac{Q}{2F} = \frac{i \cdot t}{2F} = \frac{i \cdot V/u}{2F}$$
$$\text{TOF} = \frac{|j|A}{mFN}$$

where Q is the cyclic voltammetric charge capacity obtained by integrating the CV curves, F is the Faradic constant ($96485 \text{ C}\cdot\text{mol}^{-1}$), i is the current density (A), V is the voltage (V) and u is the scanning rate ($\text{V}\cdot\text{s}^{-1}$), $|j|$ is the current density, A stands for the area of the electrode (0.1256 cm^2).

Characterization

X-ray diffraction (XRD) measurements were performed with a Panalytical X'pert PROX-ray diffractometer using a Cu $K\alpha$ source. Raman spectra were collected on a ThermoFisher DXR microscope with 633 nm laser excitation. ICP-AES analysis was performed on a Model Agilent 720. Transmission electron microscopy (TEM), high-resolution transmission electron microscopy (HRTEM) and corresponding energy dispersive spectroscopy (EDS) mapping analyses were performed with a JEOL-2100F system working at 200 kV. Scanning electron microscopy (SEM) images were recorded by a Hitachi S-4800 instrument operated at an accelerating voltage of 15 kV. X-ray photoelectron spectroscopy (XPS) measurements were carried out with AMICUS ESCA 3400 with $K\alpha$ radiation. N_2 adsorption/desorption analysis was performed at 77 K using a Micromeritics ASAP 2420 instrument. The microporous structure

information was measured by HK method, the mesoporous structure information was measured by BJH method, and the specific surface area was measured by BET method.

XAFS measurements

The X-ray absorption fine structure spectra data were collected at 1W1B station in Beijing Synchrotron Radiation Facility (BSRF, operated at 2.5 GeV with a maximum current of 250 mA). The data were collected in fluorescence excitation mode using a Lytle detector. All samples were pelletized as disks of 13 mm diameter with 1 mm thickness using graphite powder as a binder.

The acquired EXAFS data were processed according to the standard procedures using the ATHENA module implemented in the IFEFFIT software packages. The EXAFS spectra were obtained by subtracting the post-edge background from the overall absorption and then normalizing with respect to the edge-jump step. Subsequently, the $\chi(k)$ data were Fourier transformed to real (R) space using a hanning windows ($dk=1.0 \text{ \AA}^{-1}$) to separate the EXAFS contributions from different coordination shells. To obtain the quantitative structural parameters around central atoms, least-squares curve parameter fitting was performed using the ARTEMIS module of IFEFFIT software packages.

The following EXAFS equation was used:

$$\chi(k) = \sum_j \frac{N_j S_0^2 F_j(k)}{k R_j^2} \exp[-2k^2 \sigma_j^2] \exp\left[\frac{-2R_j}{\lambda(k)}\right] \sin[2k R_j + \phi_j(k)]$$

S_0^2 is the amplitude reduction factor, $F_j(k)$ is the effective curved-wave backscattering amplitude, N_j is the number of neighbors in the j^{th} atomic shell, R_j is the distance between the X-ray absorbing central atom and the atoms in the j^{th} atomic shell (backscatterer), λ is the mean free path in \AA , $\phi_j(k)$ is the phase shift (including the phase shift for each shell and the total central atom phase shift), σ_j is the Debye-Waller parameter of the j^{th} atomic shell (variation of distances around the average R_j). The functions $F_j(k)$, λ and $\phi_j(k)$ were calculated with the ab initio code FEFF8.2. The obtained S_0^2 was fixed in the subsequent fitting. While the internal atomic distances R , coordination numbers N , Debye-Waller factor σ^2 , and the edge-energy shift ΔE_0 were allowed to run freely.

DFT calculations

All geometric optimization and energy calculations were based on the VASP code³⁷. The projector augmented wave (PAW) pseudopotentials were used to describe the interaction between valence electrons and cores^{38,39}. The GGA-PBE functional was applied to express the exchange correlation interactions⁴⁰, and the kinetic cutoff energy in the plane wave basis set was set to be 520 eV. The convergence criteria of the electronic self-consistent iteration step and the ion optimization step were 10^{-5} eV and 0.03 eV/Å, respectively. Based on the XAS results, four basic catalyst models such as CN, TeC₄, CoN₄, and CoN₃C₁TeN₁C₃ were constructed (Fig. S32). A vacuum of 15 angstroms was set to avoid the virtual image interaction for all models involved in the calculation⁴¹. The gamma-centered $2 \times 2 \times 2$ k-point samplings and $5 \times 5 \times 5$ k-point samplings were used in the structure optimization and the calculation of the density of states, respectively.

The charge density difference images were visualized by VESTA software, and the calculation formula is as follows:

$$\Delta\rho(r) = \rho_{SF}(r) + \rho_{SACS}(r) - \rho_{SF+SACS}(r)$$

Where $\Delta\rho(r)$ is the charge density difference, $\rho_{SF}(r)$ is the charge density of the initial surface, $\rho_{SACS}(r)$ is the charge density of single atom (s), and $\rho_{SF+SACS}(r)$ is the charge density of the whole system.

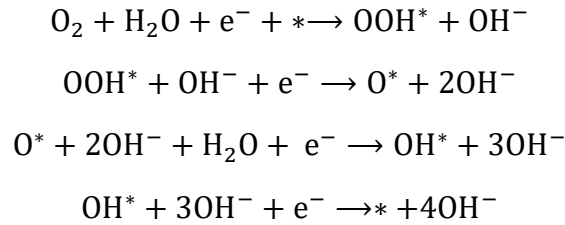
In order to explain the rationality of the calculation models at the theoretical level, the Bader charge and single-atom (s) adsorption energy of the model were calculated. The single-atom (s) adsorption energy is defined as:

$$E_b = E_{SF} + E_{SACS} - E_{SF+SACS}$$

Where E_b is the adsorption energy of single atom (s), E_{SF} is the energy of the initial surface, E_{SACS} is the energy of single atom (s), and $E_{SF+SACS}$ is the energy of the whole system. Therefore, the model is more stable when the value of the adsorption energy is more positive and higher than the cohesion energy of adsorbed atoms (the cohesion energy is defined as the difference between the average energy of free atoms and the average energy of bulk atoms)⁴², as shown in Table S1. In the meanwhile, the adsorption energy of H₂O is defined as $E_{ads} = E_{SF+WATER} - E_{WATER} - E_{SF}$, which means the energy

difference between the final H₂O adsorption state and the initial state before H₂O adsorption.

The HER free energy diagram of the catalyst at pH = 0 and the four-electron ORR reaction free energy diagram of the catalyst at pH = 13 were calculated according to the CHE model proposed by Norscov et al.^{43,44}. The free energy of hydrogen adsorption ΔG_{H^*} was adopted to describe the activity of the acidic HER process, and the water dissociation kinetic barriers in the alkaline HER were determined by the CI-NEB^{45,46} and dimer⁴⁷ methods. Besides, the theoretical overpotential for a given catalyst was used to describe the activity of ORR and determined by the minimum free energy change of the four proton-electron transfer steps. The ORR reaction path under alkaline conditions follows the four-electron associative mechanism⁴⁸:



The free energy of each step is defined a $\Delta G = \Delta E_{\text{DFT}} + \Delta \text{ZPE} - T\Delta S$, here ΔE_{DFT} is the reaction energy, ΔZPE is the difference in zero point energies, and ΔS is the change in entropy. The equilibrium potential of the four-electron ORR process under alkaline conditions was set to be 1.23 V vs. RHE as same as that under acidic conditions⁴⁸. Since the adsorption free energy of OH (ΔG_{OH^*}) is a critical factor to determine the ORR activity, and the higher of that means the weaker adsorption of OH, the ΔG_{OH^*} is then calculated as:

$$\Delta G_{\text{OH}^*} = G_{\text{OH}^*} - E_{\text{SF}} - G_{\text{OH}^-}$$

References

1. Sun, T., Zhang, S., Xu, L., Wang, D. & Li, Y. An efficient multifunctional hybrid electrocatalyst: Ni₂P nanoparticles on MOF-derived Co, N-doped porous carbon polyhedrons for oxygen reduction and water splitting. *Chem. Commun.* **54**, 12101-12104 (2018).

2. Wang, Y. et al. Hierarchical peony-like FeCo-NC with conductive network and highly active sites as efficient electrocatalyst for rechargeable Zn-air battery. *Nano Res.* **13**, 1090-1099 (2020).
3. Chen, K. et al. Iron-incorporated nitrogen-doped carbon materials as oxygen reduction electrocatalysts for zinc-air batteries. *Chinese J. Catal.* **41**, 858-867 (2020).
4. Yang, T., Cui, C., Rong, H., Zhang, J. & Wang, D. Recent advances in platinum-based intermetallic nanocrystals: Controlled synthesis and electrocatalytic applications. *Acta Phys. -Chim. Sin.*, 2003047 (2020).
5. Jing, T., Liang, D., Hao, J., Deng, M. & Cai, S. Single Pt atoms stabilized on Mo₂TiC₂O₂ for hydrogen evolution: A first-principles investigation. *J. Chem. Phys.* **151**, 24702 (2019).
6. Pan, Y. et al. Electronic structure and d-band center control engineering over M-doped CoP (M=Ni, Mn, Fe) hollow polyhedron frames for boosting hydrogen production. *Nano Energy.* **56**, 411-419 (2019).
7. Sun, K. et al. Design of basal plane active MoS₂ through one-step nitrogen and phosphorus co-doping as an efficient pH-universal electrocatalyst for hydrogen evolution. *Nano Energy.* **58**, 862-869 (2019).
8. Yu H. et al. Zn-doped Co₉S₈ nanomaterials: Preparation and application for supercapacitor and hydrogen evolution reaction of electrocatalysis. *Chinese J. Inorg. Chem.* **36**, 1318-1326 (2020).
9. Chen, Y. et al. Millisecond synthesis of CoS nanoparticles for highly efficient overall water splitting. *Nano Res.* **12**, 2259-2267 (2019).
10. Zhao, X., Luo, D., Wang, Y. & Liu, Z. Reduced graphene oxide-supported CoP nanocrystals confined in porous nitrogen-doped carbon nanowire for highly enhanced lithium/sodium storage and hydrogen evolution reaction. *Nano Res.* **12**, 2872-2880 (2019).
11. Liu, L., Zhang, J., Ma, W. & Huang, Y. Co/N co-doped graphene-like nanocarbon for highly efficient oxygen reduction electrocatalyst. *Sci. China Mater.* **62**, 359-367 (2019).
12. Fei, H. et al. Atomic cobalt on nitrogen-doped graphene for hydrogen generation.

Nat. Commun. **6**, 8668 (2015).

13. Lyu, X. et al. Atomic cobalt on defective bimodal mesoporous carbon toward efficient oxygen reduction for zinc–air batteries. *Small Methods*. **3**, 1800450 (2019).

14. Pan, Y. et al. Regulating the coordination structure of single-atom Fe-N_xC_y catalytic sites for benzene oxidation. *Nat. Commun.* **10**, 4290 (2019).

15. Pan, Y. et al. Design of single-atom Co–N₅ catalytic site: a robust electrocatalyst for CO₂ reduction with nearly 100% CO selectivity and remarkable stability. *J. Am. Chem. Soc.* **140**, 4218-4221 (2018).

16. Wang, J. et al. Heterogeneous electrocatalyst with molecular cobalt ions serving as the center of active sites. *J. Am. Chem. Soc.* **139**, 1878-1884 (2017).

17. Chen, Y. et al. Isolated single iron atoms anchored on N-Doped porous carbon as an efficient electrocatalyst for the oxygen reduction reaction. *Angew. Chem. Int. Ed.* **56**, 6937-6941 (2017).

18. Shi, Y. & Zhang, B. Recent advances in transition metal phosphide nanomaterials: synthesis and applications in hydrogen evolution reaction. *Chem. Soc. Rev.* **45**, 1529-1541 (2016).

19. Lin, R., Zhang, R., Wang, C., Yang, X. Q. & Xin, H. L. TEM ImageNet training library and AtomSegNet deep-learning models for high-precision atom segmentation, localization, denoising, and deblurring of atomic-resolution images. *Sci Rep.* **11**, 5386 (2021).

20. Liu, C. et al. Constructing FeN₄/graphitic nitrogen atomic interface for high-efficiency electrochemical CO₂ reduction over a broad potential window. *Chem.* **7**, 1297-1307 (2021).

21. Sun, T. et al. Single-atomic cobalt sites embedded in hierarchically ordered porous nitrogen-doped carbon as a superior bifunctional electrocatalyst. *Proc. Natl. Acad. Sci. USA.* **115**, 12692-12697 (2018).

22. Yin, P. et al. Single cobalt atoms with precise N-coordination as superior oxygen reduction reaction catalysts. *Angew. Chem. Int. Ed.* **55**, 10800-10805 (2016).

23. Yang, L., Xu, H., Liu, H., Cheng, D. & Cao, D. Active site identification and evaluation criteria of in situ grown CoTe and NiTe nanoarrays for hydrogen evolution

- and oxygen evolution reactions. *Small Methods*. **3**, 1900113 (2019).
24. Wang, J. et al. Amorphization activated ruthenium-tellurium nanorods for efficient water splitting. *Nat. Commun.* **10**, 5692 (2019).
25. Ya-Sheng, Q., Lei, T., Zong-Gui, S., Rong-Min, D. & Wen-Mu, L. I. Structure and performance of Fe-N_x-C catalyst for oxygen reduction reaction prepared by vacuum casting method and the second pyrolysis. *Chinese J. Struct. Chem.* **37**, 937-947 (2018).
26. Zhao, D. et al. Synergistically interactive pyridinic-N–MoP sites: Identified active centers for enhanced hydrogen evolution in alkaline solution. *Angew. Chem. Int. Ed.* **59**, 8982-8990 (2020).
27. Yi, S. et al. Insights into KMnO₄ etched N-rich carbon nanotubes as advanced electrocatalysts for Zn-air batteries. *Appl. Catal. B: Environ.* **264**, 118537 (2020).
28. Wang, Q. et al. Pyridinic-N-dominated doped defective graphene as a superior oxygen electrocatalyst for ultrahigh-energy-density Zn–air batteries. *ACS Energy Lett.* **3**, 1183-1191 (2018).
29. Pan, Y. et al. Core–shell ZIF-8@ZIF-67-derived CoP nanoparticle-embedded N-doped carbon nanotube hollow polyhedron for efficient overall water splitting. *J. Am. Chem. Soc.* **140**, 2610-2618 (2018).
30. Yu, H., Wei, X. & Li, J. The XAFS beamline of SSRF. *Nucl. Sci. Tech.* **26**, 6-12 (2015).
31. Jiang, H. et al. Defect-rich and ultrathin N doped carbon nanosheets as advanced trifunctional metal-free electrocatalysts for the ORR, OER and HER. *Energ. Environ. Sci.* **12**, 322-333 (2019).
32. Wang, Y. et al. Ultrasmall NiFe layered double hydroxide strongly coupled on atomically dispersed FeCo-NC nanoflowers as efficient bifunctional catalyst for rechargeable Zn-air battery. *Sci. China Mater.* **63**, 1182-1195 (2020).
33. Han, S. C., Hu, X. Y., Wang, J. C., Fang, X. S. & Zhu, Y. F. Novel route to Fe-based cathode as an efficient bifunctional catalysts for rechargeable Zn-Air battery. *Adv. Energy Mater.* **8**, 1800955 (2018).
34. Luo, M. et al. PdMo bimetallic for oxygen reduction catalysis. *Nature*. **574**, 81-85 (2019).

35. Jiao, Y., Zheng, Y., Davey, K. & Qiao, S. Activity origin and catalyst design principles for electrocatalytic hydrogen evolution on heteroatom-doped graphene. *Nature Energy*. **1**, 16130 (2016).
36. Yue, X., Huang, S., Cai, J., Jin, Y. & Shen, P. K. Heteroatoms dual doped porous graphene nanosheets as efficient bifunctional metal-free electrocatalysts for overall water-splitting. *J. Mater. Chem. A*. **5**, 7784-7790 (2017).
37. Kresse, G. & Furthmüller, J. Efficient iterative schemes for ab initio total-energy calculations using a plane-wave basis set. *Phys. Rev. B*, **54**, 11169-11186 (1996).
38. E, B. P. Projector augmented-wave method. *Phys. Rev. B*, **50**, 17953 (1994).
39. Kresse G, J. D. From ultrasoft pseudopotentials to the projector augmented-wave method. *Phys. Rev. B*, **59**, 591758 (1999).
40. Perdew, J. P., Burke, K. & Ernzerhof, M. Generalized gradient approximation made simple. *Phys. Rev. Lett.* **77**, 3865-3868 (1996).
41. Lu, Z. et al. An isolated zinc–cobalt atomic pair for highly active and durable oxygen reduction. *Angew. Chem. Int. Ed.* **58**, 2622-2626 (2019).
42. Zhang, L. et al. Coordination of atomic Co–Pt coupling species at carbon defects as active sites for oxygen reduction reaction. *J. Am. Chem. Soc.* **140**, 10757-10763 (2018).
43. Nørskov J K, B. T. L. A. Trends in the exchange current for hydrogen evolution. *J. Electrochem. Soc.* **152**, J23 (2005).
44. Nørskov, J. K. et al. Origin of the overpotential for oxygen reduction at a fuel-cell cathode. *J. Phys. Chem. B*. **108**, 17886-17892 (2004).
45. Henkelman, G., Uberuaga, B. P. & Jónsson, H. A climbing image nudged elastic band method for finding saddle points and minimum energy paths. *J. Chem. Res.* **113**, 9901-9904 (2000).
46. Henkelman, G. & Jónsson, H. Improved tangent estimate in the nudged elastic band method for finding minimum energy paths and saddle points. *J. Chem. Phys.* **113**, 9978-9985 (2000).
47. Henkelman, G. & Jónsson, H. A dimer method for finding saddle points on high dimensional potential surfaces using only first derivatives. *J. Chem. Phys.* **111**, 7010-

7022 (1999).

48. Wang, J. et al. Synergistic effect of well-defined dual sites boosting the oxygen reduction reaction. *Energ. Environ. Sci.* **11**, 3375-3379 (2018).

Acknowledgements

This work was supported by the Taishan Scholars Program of Shandong Province (No. tsqn201909065), Shandong Provincial Natural Science Foundation (ZR2020QB174), PetroChina Innovation Foundation (2019D-5007-0401), the Fundamental Research Funds for the Central Universities (No. 19CX02008A), Postgraduate Innovation Fund of China University of Petroleum (East China) (No. YCX2020037).

Data availability

The authors declare that all of the data supporting the findings of this study are available within the paper and the Supplementary Information, and also from the corresponding authors upon reasonable request. Source data are provided with this paper.

Author contributions

M. W. and Y. P. designed the project, and wrote the manuscript. M. W. prepared the catalyst samples, tested the HER and ORR performance, analyzed the data and wrote the corresponding sections. X. Z., X. F. and C. Y. conducted DFT calculations, analyzed the calculation data, wrote the corresponding section and participated in revising the manuscript. M. L. tested the HER performance. K. S. and W. C. C. conducted HAADF STEM-EDS mapping experiments. C. L. designed and carried out the XAS experiments. Z. L. and Y. C analyzed and fitted all the XANES and EXAFS data. S. L. tested, analyzed and fitted all the XANES and EXAFS data. B. W. tested the Zn-air battery performance. Y. L. conducted TEM experiments. Y. P., Y. L., C. L. and

C. C. supervised the project, directed the research and established the final version of the manuscript. M. W. and X. Z. contributed equally to this work.

Additional information

Supplementary information is available for this paper. Reprints and permissions information is available at www.nature.com/reprints. Correspondence and requests for materials should be addressed to Y. P.

Competing interests: The authors declare no competing interests.

Supplementary Files

This is a list of supplementary files associated with this preprint. Click to download.

- [SupportingInformationforNatureCommunication.docx](#)